



LAWRENCE
LIVERMORE
NATIONAL
LABORATORY

LLNL-TR-401597

Developing High Energy Radiography for HED Experiments on NIF and Omega-EP

B. Maddox, R. Tommasini, B. Remington, M. Key,
R. Town

February 22, 2008

Disclaimer

This document was prepared as an account of work sponsored by an agency of the United States government. Neither the United States government nor Lawrence Livermore National Security, LLC, nor any of their employees makes any warranty, expressed or implied, or assumes any legal liability or responsibility for the accuracy, completeness, or usefulness of any information, apparatus, product, or process disclosed, or represents that its use would not infringe privately owned rights. Reference herein to any specific commercial product, process, or service by trade name, trademark, manufacturer, or otherwise does not necessarily constitute or imply its endorsement, recommendation, or favoring by the United States government or Lawrence Livermore National Security, LLC. The views and opinions of authors expressed herein do not necessarily state or reflect those of the United States government or Lawrence Livermore National Security, LLC, and shall not be used for advertising or product endorsement purposes.

This work performed under the auspices of the U.S. Department of Energy by Lawrence Livermore National Laboratory under Contract DE-AC52-07NA27344.

Developing High Energy Radiography for HED Experiments on NIF and Omega-EP

Final report for DNT LDRD, 05-ERD-006

PI: Hye-Sook Park, NIF/ICF

Collaborators: B. Maddox, R. Tommasini, B. Remington, M. Key, R. Town

ABSTRACT

High energy radiography capabilities are essential for many future DNT/HED experiments on NIF. We have been developing bright, high-energy (15-100 keV), high resolution ($< 20 \mu\text{m}$), 1-D and 2-D radiography solutions for DNT experiments on NIF. In this LDRD, we have made significant progress utilizing high-energy, high-intensity, short-pulse lasers to generate hard K- α photons. High energy K- α sources are created by hot electrons interacting in the target fluor material after irradiation by lasers with intensity $I_L > 10^{17} \text{ W/cm}^2$. High resolution point projection 1-D and 2-D radiography have been achieved using μ -foil and μ -wire targets attached to low-Z substrate materials. The μ -wire size was $10 \times 10 \times 300 \mu\text{m}$ on a $300 \times 300 \times 5 \mu\text{m}$ CH substrate creating the point source size equivalent to these micro targets. This unique technique will utilize the NIF short pulse laser (ARC) as a backlighter suitable for the full range of DNT science experiments on NIF.

I. INTRODUCTION

X-ray radiography using backlighter sources has been an important tool for diagnosing and imaging various stages of planar and convergent hydrodynamics for laser experiments. Current experiments at Omega utilize $E_x < 9 \text{ keV}$ backlighters emitted by thermal plasmas. However, many planned high energy density (HED) experiments on new laser facilities such as the Omega-Extended performance (EP)¹, Z Refurbishment (ZR)², and the National Ignition Facility (NIF)³ will require backlighters that can probe high areal density materials with high resolution.

Such research includes the study of material strength under

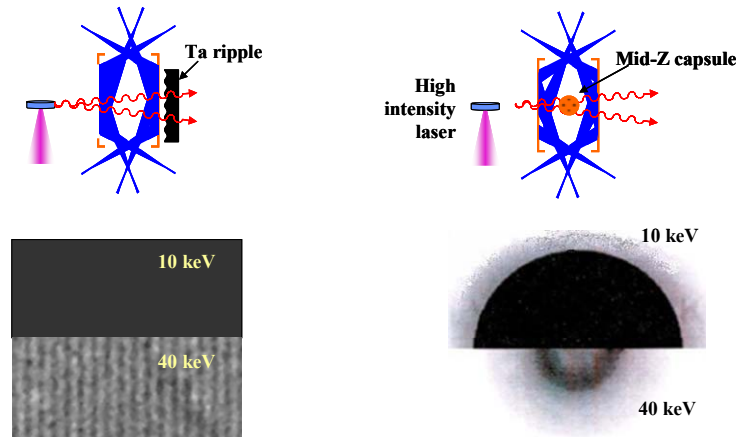


Fig 1. Examples of high energy density experiments that require high energy backlighters on NIF. The left panel is for the material strength experiment where the ripple growth factors are measured via face-on radiography. (b) The right panel is the mid to high-Z capsule implosion experiments where capsule implosion symmetry will be studied. All require $>40 \text{ keV}$ radiography due to high areal density and the sample thickness.

high pressure⁴ and mid to high Z capsule implosion experiments⁵ as depicted in Fig 1. In a material strength experiment, an artificially induced sinusoidal rippled sample material is compressed by a laser piston drive⁶, then, radiograph the ripple growth at 10's of ns after the drive. By measuring the growth rate from the radiographs and using the properties of the Rayleigh-Taylor instability, we can derive the material strength parameters under high pressure. In this experiment, the backlighter x-ray energy is dictated by the sample material types and their thicknesses. For Al or Vanadium samples of $\sim 35 \mu\text{m}$ thickness, 4.3 keV or 5.2 keV backlighters are sufficient to obtain high contrast radiographs of ripple growth factors of ~ 10 . On NIF, we plan to study Ta or other high-Z materials of $\sim 100 \mu\text{m}$ thickness. In this case, we will need a backlighter of $>40 \text{ keV}$. The second example is radiography of imploding capsules that are made of mid to high-Z materials. Unlike the CH or Be ignition capsules, these mid-Z capsules will have high areal core densities when they are compressed. Again, we will need $>40 \text{ keV}$ backlighter to image spatial features on these targets.

The K- α emission mechanism using high intensity lasers is a promising way of creating 17-100 keV high energy photons. When a laser with intensity $>10^{17} \text{ W/cm}^2$ strikes a target, a forward directed "spray" of energetic electrons is created, with energies as high as $\sim 100 \text{ MeV}$ ⁷. This forward current draws a return current, and a very strong azimuthal magnetic field is created, with a strength predicted to be 10-100 MG or higher. As these energetic electrons traverse the target, bound electrons can be knocked out by electron-electron scattering. If a K-shell electron is knocked out, this inner shell vacancy is quickly filled by an L-shell or M-shell electron, generating isotropic K- α or K- β radiation.

We have demonstrated that the high energy x-ray generated by high intensity lasers is confined to within the target material and that high resolution 1-D radiography can be achieved by irradiating a thin μ -foil viewed edge-on⁸. As illustrated in Fig 2, the spatial resolution for this edge-on 1-D radiography is determined by the μ -foil thickness as the x-ray source generation is confined to the μ -foil (Fig 2a). Utilizing these properties, we demonstrated 40 keV 1-D radiography by irradiating small Samarium foils of $100 \mu\text{m} \times 100 \mu\text{m} \times 5 \mu\text{m}$ thickness viewed edge-on. 2-D radiography has been tested with various small wire targets buried in different geometric shapes such as an embedded wire in a low-Z substrate and a wire attached to a low-Z cone to create a small point source for 2-D radiography (Fig 2b). We studied the limiting spatial resolution from these edge-on sources and the backgrounds associated with them.



Fig 2. Sketch of the point projection radiography using μ -foil source with $\sim 5 \mu\text{m}$ thin for 1-D and μ -wire source with $\sim 10 \times 10 \times 300 \mu\text{m}$ wire for 2-D radiography. In the high energy K- α radiography, the x-ray radiation is confined within the fluor target material. Usage of reduced mass target enables to produce high resolution radiography.

II. RESEARCH ACTIVITIES

We performed several experiments using many short pulse laser facilities such as Vulcan lasers at the Rutherford Appleton Laboratory in UK, and the Titan laser to demonstrate high-energy radiography. These short pulse laser uses chirped-pulse amplification⁹, or CPA, to generate short-pulse (1-50 ps), high- power (100TW) beams. In a typical CPA system a short (10 – 200 fs), low energy (~ 1 nJ) pulse is generated by a mode-locked oscillator in the front end. This short pulse is stretched in time to ~ 3 ns then amplified to the \sim Joule level. In the final stage of CPA, the amplified, chirped pulse is temporally compressed back to its original duration. The output of compressed pulse is then focused via an off-axis f/3 parabola creating a small laser spot. The small spot size and the short pulse duration create high intensity beams of 10^{16} W/cm² to 10^{19} W/cm².

Utilizing these lasers we measured the $K\alpha$ yields from various wire targets and studied their dependence on laser intensities, target material types, target thickness etc. We also tested different imaging detectors suitable for high energy radiography. These are Image Plates and CsI or Gd₂O₂S scintillators mated to a CCD camera. In order to understand the physics issues associated with hot electron flow for the cone/wire targets and embedded wires, we began to develop integrated modeling capability with PIC/LSP.

The following sections describe the highlights of our experimental results.

III. RESULTS AND TECHNICAL OUTCOME

III.1. Experimental Setup

A schematic of the Titan experiment is given in Fig 3. The μ -flag or μ -wire radiography targets were placed at the focal spot and rotated precisely to give an edge-on view to the imaging detectors at 2 locations. We employed 2 different types of high energy x-ray imaging techniques: the first one used Image Plates and the other technique used a Gd₂O₂S/CCD electronic imager fabricated by Roper Scientific. In this set-up, the angle between the incident backlighter laser and the detectors was 16 degrees for the Gd₂O₂S/CCD detector and 40.7 degrees for the image plate detector.

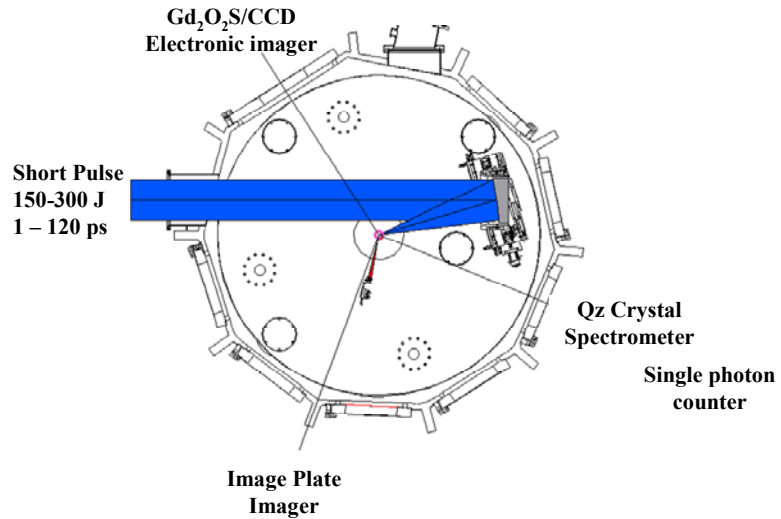


Fig 3. Titan experimental set-up. Two different types of imaging device (Image Plate and Gd₂O₂S/CCD imager) and two different spectrometers (single photon counting camera and dual crystal spectrometer) were employed to measure radiography spatial resolution and the K- α conversion efficiencies.

III.2. Detectors

Image Plate Detector: Image plates detect incoming x-ray photons on a uniform layer of small grain BaFBrI crystals¹⁰. Excited electrons are trapped by empty halogen ion sites in the crystal, making metastable color centers capable of emitting radiation. Irradiation by a laser beam absorbed by the color centers excites the electrons again which quickly recombine with holes, and the recombination energy is transferred to the I ions, resulting in photo stimulated luminescence. For our experiment we use the BAS-SR type image plates manufactured by Fujifilm.

Gd₂O₂S/CCD Detector: The other imaging detector was a terbium-doped gadolinium oxysulfide (Gd₂O₂S:Tb) scintillator that coupled to a CCD camera. The scintillator converts incoming x-rays into ~550 nm optical photons that are collected by the CCD detector.

Single photon counting camera: In addition to the imaging detectors, we also used 2 different types of spectrometers. The first one is a single photon counting camera. This is a CCD camera that absorbs the x-ray photons directly in the silicon depletion region. When an x-ray photon is fully absorbed within a pixel, photo electrons are created. For a silicon CCD, the pair creation energy is 3.65 eV at room temperature; a 1 keV x-ray photon, if absorbed completely in one pixel, will produce 274 photoelectrons (pe). The number of pe's collected on a pixel, then, is proportional to the incoming x-ray energy. Because of the fairly thin (16 μ m) depletion layer of readily available CCDs, this detector is sensitive only up to ~30 keV.

Qz crystal spectrometer: The second spectrometer is a transmission crystal in Laué geometry. This instrument uses a Qz(10-11) crystal curved to a radius of 254 mm¹¹. The curvature of the crystal focuses photons onto the image plate. With this spectrometer we were able to detect up to 80 keV photons with a spectral resolution of >300.

III.3. Laser Target

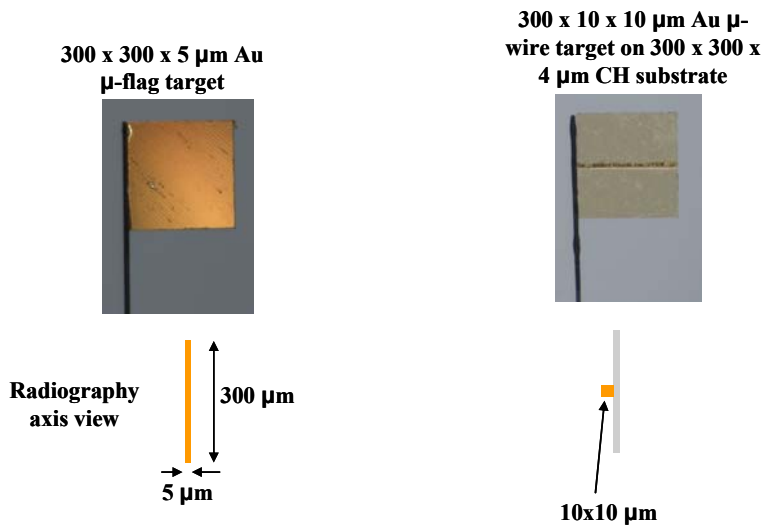


Fig 4. Fabricated μ -foil and μ -wire targets. These are the examples for Au K- α radiography. We have tested Mo, Ag and Sm targets that are fabricated similarly. The radiography axis is the edge-on view where the x-ray radiation view is micro wire or micro dot.

Building on our demonstration that high energy x-ray generation can be confined to within a target volume; we made μ -foil and μ -wire targets mounted on top of low-Z substrates to create small point sources for 1-D and 2-D radiography. Fig 4 shows an example of Au μ -foil and Au μ -wire targets. These targets were fabricated by General Atomics. The μ -foil is a simple 300x300x5 μ m Au foil held by a Carbon fiber 6 μ m diameter. The edge of this foil is cleanly sheared

so that very little slag is seen from the edge-on view. Similar targets, made of Mo, Ag and Sm have also been tested in our experiments.

The μ -wire target was difficult to fabricate. The K- α radiator material (Au for instance) was deposited on top of the $4 \sim 5 \mu\text{m}$ thin CH substrate; then micro-machined into a small wire-like volume. We chose CH as the substrate in order to reduce Bremsstrahlung background. We chose the micro-machining process (instead of gluing a wire on to the substrate) so that the μ -wire has better contact with the substrate. The short pulse laser hits on the μ -wire side. Typically the short pulse laser deposits only $\sim 58\%$ of its total energy on the $10 \mu\text{m}$ wire at its best focus. The substrate plays the role of guiding the hot electrons towards the fluor material.

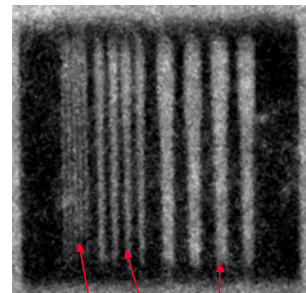
III.4. 40 keV 1-D radiography with a μ -flag targets

We performed proof-of-principle laser shots to demonstrate the edge-on 1-D radiography concept. The $100 \times 100 \times 5 \mu\text{m}$ samarium (Sm) foils were prepared by laser cutting to the square shape and mounting on a $6 \mu\text{m}$ carbon fiber stalk, as shown in the figure. Since 1-D edge-on radiography relies on having a minimum lateral (edge-on) cross section, care had to be taken to cut the edges cleanly and to mount the foils so that they were flat. To minimize sensitivity to tilt, one would like very small foils. Finite laser pointing accuracy, however, prevents the disks from being too small. The $100 \times 100 \mu\text{m}$ target size was a compromise between these two considerations. Fortunately due to the electron refluxing mechanism, the overall K α emitted flux is not sensitive to foil thickness or lateral extent, to first order. Note that the mean free path length of the 40 keV K α x-rays in cold Sm is $\sim 200 \mu\text{m}$; so the x-ray re-absorption is minimal.

We fabricated special slits made of $12 \mu\text{m}$ thick Ta and Au substrates. These slits were made by laser cutting and they had 20, 40, 80 and $160 \mu\text{m}$ periods. Then, we added a 35 to $37 \mu\text{m}$ thick Ta or Au substrate behind the $12 \mu\text{m}$ thick resolution slits. This is to simulate the expected optical depths of typical targets anticipated for laser experiments at NIF or other facilities. The distance between the laser target, the Sm edge-on foil, and the resolution radiography object was set to 3~4 cm while the desired imaging magnification is 10 to 15 for optimal signal per resolution element. We used a $200 \mu\text{m}$ thick Sm foil as a filter to transmit 40 keV K α radiation while

greatly reducing the lower energy and higher energy background creating a quasi-monochromatic transmission.

Figure 5a shows the resulting radiography image of the Ta slits with the CsI/CCD camera using the Vulcan TAW laser. The laser energy was 75 J for Ta with a 10 ps pulse



Period of 20 μm , 40 μm , 80 grids

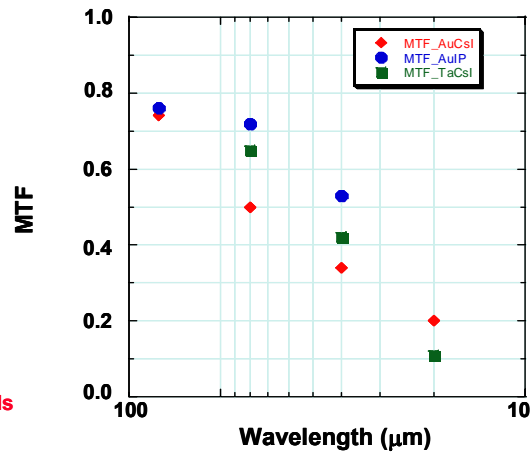


Fig 5. 1-D 40 keV radiography results. Period of 20 mm grid lines are resolved with a MTF of $\sim 20\%$ with 60J short pulse laser.

duration. For the 1-D radiography analysis, we summed and averaged the pixel intensity values along the slits to increase the signal-to-noise ratio. The resulting lineouts are shown in Figure 9d. All the resolutions patterns are clearly visible down to the 20 μm period slits in the CsI/CCD camera data.

Since our resolution patterns are square form rather than sinusoidal, from this lineout data we calculated the modulation transfer function (MTF) using a contrast transfer function (CTF) definition⁵¹. The modulation transfer function is derived by:

$$MTF(f) = \pi/4 [CTF(f) + CTF(3f/3) - CTF(5f/5) + CTF(7f/7)...]$$

Figure 5b shows the resulting MTF from different slit sizes and many different laser shot images. The spatial resolution, as quantified by the average MTF, was approximately 0.15, 0.4, 0.6, and 0.75 at $\lambda = 20, 40, 80,$ and $160 \mu\text{m}$, respectively. The image contrast, MTF, also depends on the signal to noise ratio (SNR). By scaling the laser energy from our experiment, we expect to have at least 7 times more signal and 2.5 times higher SNR at NIF, assuming the noise is mostly from photon statistics. In addition the angular alignment was only good to $\sim 1^\circ$ for the premounted targets in these experiments, which degrades the resolution measurements. This alignment accuracy can clearly be improved. With these improvements, we expect to be able to obtain higher MTF for future experiments on NIF-ARC and Omega-EP.

III.5. 22 keV 2-D radiography with a μ -wire targets

In order to demonstrate 2-D radiography, we fabricated a test pattern that consists of an orthogonal stack of 1-dimensional slits (10, 20, 30, 40, 80 μm) on a 25 μm thick Au substrate. This test pattern was fabricated by a mask projection technique using an Excimer laser¹².

Using this pattern, we tested the performance of a 2-D radiography Ag μ -wire target that produces 22 keV k- α x rays. The laser energy for this shot was 242J with a 40 ps pulse duration. We defocused the laser to have 50% of laser energy contained within a 54 μm radius area. The resulting radiograph is shown in Fig 6. The diagonal sections with 10, 20 and 30 μm grids are denoted in the figure. With a 10 μm source size, we expected to resolve no better than 10 μm features as seen in this image. This image is taken with the Gd₂O₂S/CCD detector with an imaging magnification of 17.

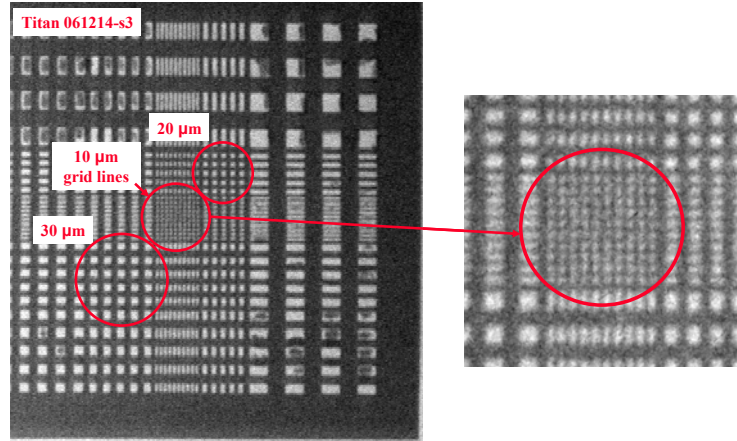


Fig 6. The results of Ag K- α radiography with m-wire target. The diagonal sections with 10, 20 and 30 μm grids are denoted. The central 10 μm grid region is well resolved.

We further analyzed this image to obtain the point spread function. , We first created an ideal grid image by differentiating in the vertical and horizontal directions the image of a small, 30 μ m grid section. This ideal grid image was smeared by a Gaussian function until it fit the data best as shown in Fig 7a. The resulting fit to the sigma of a Gaussian point spread function yields 4.3 μ m. This is consistent with the μ -wire size of 10 μ m and proves that the high energy x-ray photons come mainly from the μ -wire and that the spatial resolution is limited by the μ -wire size. With this fit point spread function, we calculate the modulation transfer function (MTF) through:

$$M(k) = e^{-(k\sigma)^2/2}, \text{ where } k = \frac{2\pi}{\lambda}$$

Here M(k) is the MTF, σ is the above fit point spread function parameter, λ = the periods of the modulation. The resulting M(k) is plotted in Fig 7b. From this plot we deduce that we can achieve a 30% modulation for 20 μ m spatial features. This experiment was conducted with a laser energy of \sim 250 J. The MTF is expected to be higher with a stronger laser..

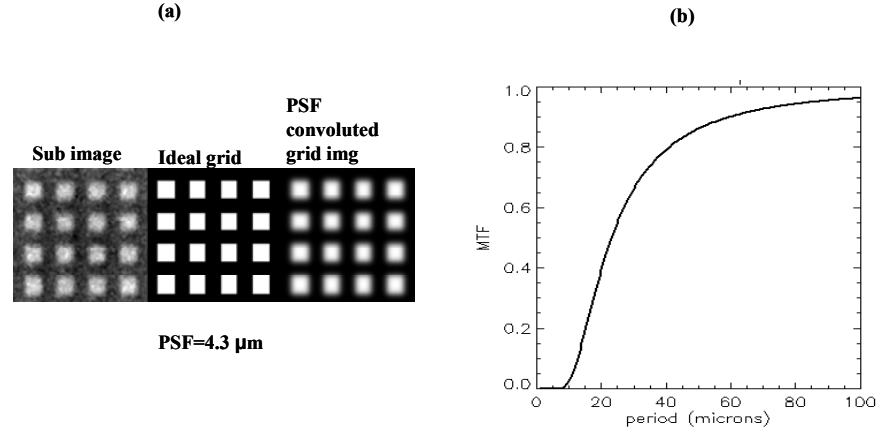


Fig 7. MTF analysis of the radiography in Fig 6. The point spread function is obtained by finding the best match of the data with an ideal grid image convoluted with the point spread function. We obtain \sim 40% MTF at 20 μ m periods with 250J Titan laser. When applied to higher energy lasers, we expect to improve the MTF.

III.6. 68 keV 1-D and 2-D radiography with m-foils and μ -wire targets

We have also tested Au K- α backlighter targets for 68 keV radiography in the μ -foil and μ -wire geometries, Fig 9a. For 68 keV radiography, the Au grid test pattern (25 μ m thick Au substrate) used to test radiography at 22 keV, was inadequate as the attenuation length of Au at 68 keV is 163 μ m. Instead, we measured the resolution using 1 mm thick Au plates that had several channels carved all the way through by EDM (Electrical Discharge Machining.) The edges of the channels served as knife-edge targets for testing resolution and the EDM process minimized any slag that could be seen when viewed edge-on (Fig 9b).

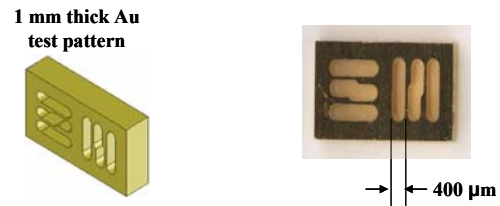


Fig 8. Test target for Au radiography (68 keV). The target is made of 1 mm thick Au material with EDM edges.

Two radiographs from these experiments are shown in Fig 9. The laser parameters used for these shots were similar to the settings used for the 22 keV Ag radiography described above. Fuji BAS-SR type image plates were used to record these images. Fig 9a was taken with a 1-D μ -flag target positioned in the vertical plane, perpendicular to the image. The 1-D nature of the spatial resolution is clear; the spatial resolution is good only in the horizontal

direction and only near the center of the image where the image plate sees only the edge of the target and not its sides. Fig 9b was taken with a μ -wire target pointed at the image plate. Unlike the μ -foil target this image shows good spatial resolution in all directions. To quantify the spatial resolution, we fit lineouts across the edges (Fig 9b) to an edge spread function (ESF). The ESF is the integral response function of a Gaussian point spread function (PSF) which fits our knife-edge data well when combined with a linear background term:

$$ESF = I_0 \cdot \text{erf}\left(\frac{x}{\sigma}\right) + a_0 + a_1 x$$

where,

$$\text{erf}\left(\frac{x}{\sigma}\right) = \frac{2}{\pi} \int_0^{x/\sigma} e^{-t^2} dt$$

$I_0, \sigma, a_0, a_1 = \text{fitting coefficients}$

The fit results are shown as red lines in Fig 9a and b. From this fit, we find the FWHM of the PSF to be $10.7 \pm 1.0 \mu\text{m}$ in the 1-D image and $12.3 \pm 1.2 \mu\text{m}$ in the 2-D image, respectively. These measured numbers are larger than the actual foil thickness of $5 \mu\text{m}$ and wire size of $10 \mu\text{m}$. This is likely caused by alignment errors of the thick test pattern target. After taking our 0.5° alignment accuracy into account, the resulting FWHM is consistent with the physical thickness of the μ -foil.

In this direct comparison of μ -foil and μ -wire radiography, it is clear that the K- α emission is confined to within the fluor material and any plasma blow-off or substrate emission does little to degrade the spatial resolution.

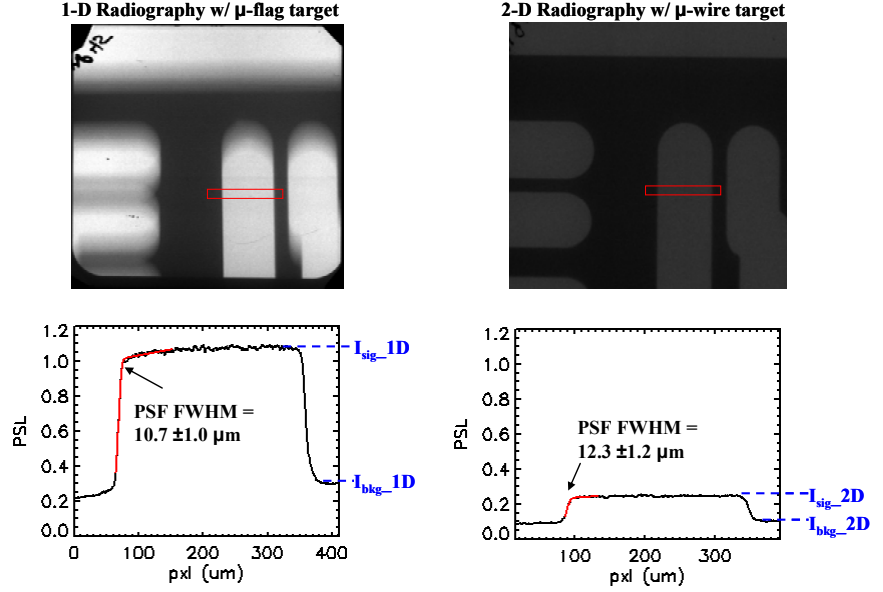


Fig 9. Radiography results from the Au μ -flag and μ -wire targets. 1-D and 2-D natures are clearly detected. The edges were fitted the edge spread function and the radiometric difference are explained in the text.

III.7. Radiometric intensities of μ -flag and μ -wire sources

The differences in relative photon output between the μ -flag and μ -wire targets were apparent in these experiments. The images are presented in PSL units which linearize the image plate scanner output digital scale [ref]. We denote the signal levels in the lineouts by $I_{\text{sig_1D}}$ and $I_{\text{sig_2D}}$ and the background levels by $I_{\text{bkg_1D}}$ and $I_{\text{bkg_2D}}$. We measure $I_{\text{sig_1D}}=1.08 \pm 0.03$, $I_{\text{bkg_1D}}=0.21 \pm 0.15$, $I_{\text{sig_2D}}=0.25 \pm 0.018$ and $I_{\text{bkg_2D}}=0.088 \pm 0.011$. From these numbers we deduce that the number of x-ray photons emitted by the source and captured by the image plates is 4 times higher for the 1-D μ -flag targets than for the 2-D μ -wire targets.

The difference may be explained by the size of the area on the fluor intersected by the laser. For the μ -flag target, 100% of the laser energy struck the Au material whereas for the μ -wire only 25% of the laser energy struck the Au as we operated the laser in ‘defocused’ mode for these shots. As discussed in section II, the defocused laser spot has a radius of 54 μm . If the laser spot is Gaussian, the intersection with a 10 μm diameter wire is only 25% of the total beam area.

The difference in signal level between the 1-D μ -flag targets and the 2-D μ -wire targets as measured by image plate radiography is not the same as the difference determined by measurements of the K- α yield. In Fig 10, we compare μ -flag and μ -wire target K- α spectra measured with a single photon counting camera. The μ -flag target was a 100x100x5 μm Mo foil and the μ -wire target was a 150x20x10 μm Mo wire on a 150x150x10 μm Al substrate. The laser energy was 280J and we used the best focus ($\sigma=6.2 \mu\text{m}$) to hit the μ -wire. After correcting for the filters and shot-to-shot differences in the laser energy, our measurements indicate that the number of hits in the K- α peak for the μ -wire target is 10 times less than the number from the μ -flag targets. The factor of 10 differences in K- α yields cannot be accounted for by the mass difference nor the difference in the size of the area struck by the laser. The volume of Mo in the μ -wire target is 30000 μm^3 , and the volume of Mo in the μ -flag target is 50000 μm^3 , so the two targets have similar mass. Furthermore, the μ -wire target accepts 90% of the focused laser energy. One possible explanation for this low yield may be that a high Ohmic barrier is created by the strong return current along the wire length direction ($>100 \mu\text{m}$ long), which limits the length of wire that sees the hot electron flux. The thin foils ($\leq 10 \mu\text{m}$), on the other hand, create their return current in the form of refluxing hot electrons, so the effects of an Ohmic barrier are greatly reduced.

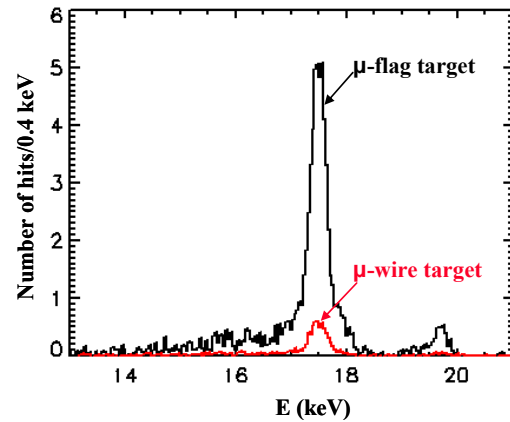


Fig 10. K- α yield difference between μ -flag and μ -wire target measured by single photon counting camera. After accounting the difference in laser energy, filter setting, we measure the K- α yield difference between these 2 types of target is a factor of 10.

III.8. Simulation

The interaction of a short-pulse laser with a solid-density target is a complex process that involves physics on different temporal and spatial scales. We have combined multiple independent simulation codes into one integrated code to perform simulations of the entire process. To model the experiments reported here we have mainly performed simulations using the LSP code¹³ that we are using to transport relativistic electrons through dense plasmas. The LSP code employs a direct implicit particle push based on an energy-conserving electromagnetic algorithm. This algorithm enables larger time steps than conventional explicit PIC codes, which operate on space and times scales given by the Debye length and plasma frequency. In LSP, electrons can be represented as kinetic, or fluid particles. In the fluid description, the electrons carry a temperature, which is advanced by a separate energy equation that greatly reduces the effect of numerical cooling. The net effect of these algorithms is to enable LSP to model larger, denser plasmas for longer simulation times than explicit PIC codes. We have recently modified the Monte-Carlo ITS kernel within LSP so that the only effect of this module is to generate photons. We have also integrated NLTE atomic physics tables from FLYCHK into LSP to calculate the charge state distribution, opacities and emissivities. These photons are transported through the target using DRAT to yield, for example, time- and space-integrated spectra, total photon yields, and K α images. This enables us to directly compare the simulation output to the experimental measurements.

Figure 11 shows a simulation for a μ -wire target. The color represents hot electron particle densities. We can clearly see that the hot electrons are confined within the target material as seen in the experiment. This simulation also predicts the absolute K- α yields that are compared to the experimental measurements.

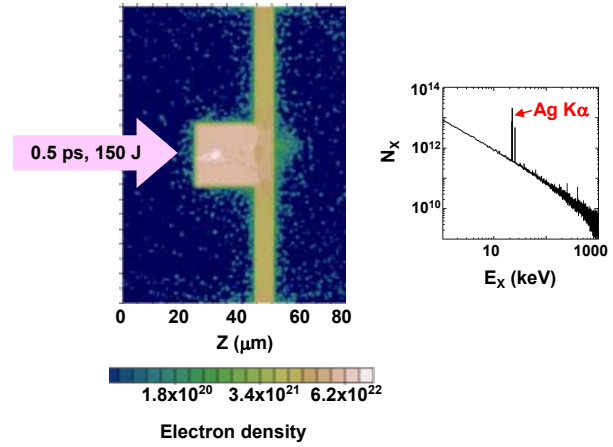


Fig 11. LSP simulation of 20x20x100 μ m Ag m-wire target. The color represents the electron density.

III.9. K- α conversion efficiencies for μ -foil targets

We measure the efficiency of converting laser energy to K- α x-rays using two different spectrometers: a single photon counting (SPC) CCD camera for K- α energies between 10 keV and 30 keV, and a quartz crystal spectrometer for K- α energies between 15 keV and 78 keV. Details of these detectors were given in section II.

Fig 12a shows an example of the spectrum of an Ag μ -wire target measured by the SPC detector. The K- α and K- β peaks are clearly visible. We count the number of hits above the background in the K- α and K- β peaks and multiply by the photon energy to obtain $E_{K\alpha}(\text{measured})$, the measured amount of K- α or K- β radiation in the detector. The conversion efficiency is, then, calculated by:

$$\epsilon_{\text{conv}} = (E_{K\alpha}(\text{measured}) \cdot 4\pi) / (\epsilon_{\text{detector}} \cdot \epsilon_{\text{single_hit}} \cdot T_{\text{filter}} \cdot \Omega_{\text{detector}}) / E_{\text{laser}}$$

where ϵ_{conv} is the conversion efficiency, $\epsilon_{detector}$ is detector quantum efficiency ϵ_{single_hit} is the probability that all of the 22 keV energy from a single photon is captured in one pixel, T_{filter} is the transmission factor through the filter materials, and $\Omega_{detector}$ is the detector solid angle. The detection efficiency for the SPC is absolutely calibrated using a Cd109 radioactive source¹⁴. The calibration allows us to determine the combined efficiency $\epsilon_{detector} \times \epsilon_{single_hit}$ to be 5% for Cu K α and 0.3% for Ag K α . Knowing these efficiencies allows us to measure the absolute conversion efficiencies for Cu, Mo, Ag, and Sn targets with this detector.

For the higher Z target materials we use the crystal spectrometer. Fig 12b shows data for Sn, Sm, Ta, Au and Pb target materials. Again we count the number of hits above the background. The detector (image plate) response is calculated assuming that the BaFBr:I phosphor material is 120 μm thick, then using the standard energy dependent x-ray absorption coefficients for this material. The Qz

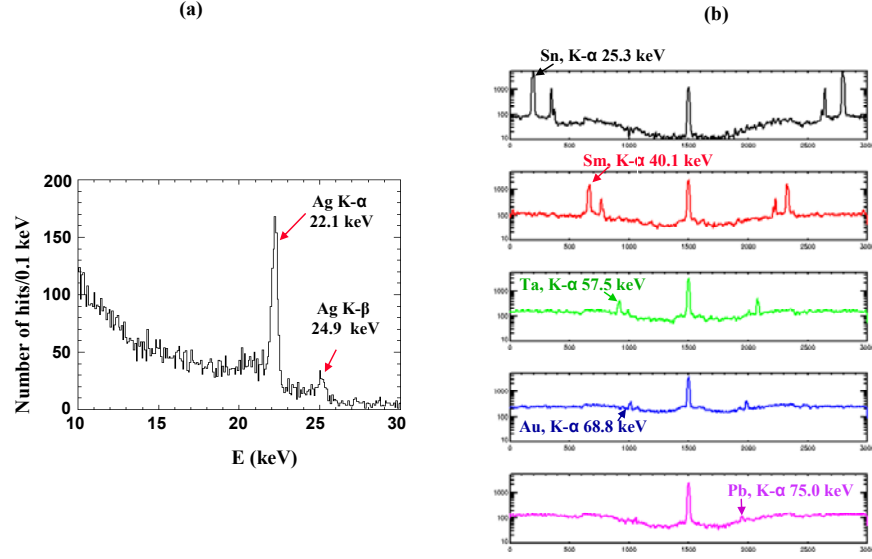


Fig 12. K- α yield measurements using single photon counting camera (a) and the dual crystal spectrometer (b) for various target materials. We measure the absolute K- α conversion efficiencies using the single photon counting camera at 8 to 25 keV and the relative conversion efficiencies using the dual crystal spectrometer at 20 to 80 keV. By normalizing the K- α efficiencies at 22 keV, we measure the K- α efficiencies from 17 to 75 keV.

crystal response is extrapolated from XOP simulation results¹⁴. This procedure gives only a relative response function for the crystal spectrometer. Since both the crystal spectrometer and the SPC can measure Ag K- α photons the relative responses of the crystal spectrometer were scaled so that the measurement of the Ag K- α made by the two instruments agreed. This provided an absolute calibration of the crystal spectrometer for the other measurements. The resulting conversion efficiencies are plotted in Fig 12.

We compare these results with Monte Carlo (MC) simulation. The MC simulation of K α x-ray production proceeds in two steps. First, a hot electron temperature is determined from the formula $T_{hot} = 130 \text{ keV} (I(\text{W}/\text{cm}^2)/10^{17})^{1/2}$ ¹⁶ at each laser intensities of interest. Electrons are then generated having energies taken from the Boltzman distribution characteristic energy. Each electron is then transported through the target material using the ITS (Integrated Tiger Series) Monte Carlo code. In the calculation, the electrons are emitted at the surface of the solid target into a cone of half-angle 26° into the target. The ITS simulation determines the number of K α x-ray photons per hot electron per steradian as a function of angle. We use the hot electron conversion efficiency of $\sim 12\%$ at $2 \times 10^{18} \text{ W}/\text{cm}^2$ measured by Yasuike et al¹⁶ to determine the

number of hot electrons as a function of laser intensity. By multiplying the yield of K- α photons per electron per steradian from the first step by the number of hot electrons from the second step, we obtain the K- α yield per steradian.

The resulting output of the MC simulations is noted as the red line in Fig 13. The current simulation set doesn't account for electron refluxing¹⁷ which can increase K- α production. Note that we have normalized the simulated conversion efficiencies so that it matches the well measured Ag K- α data.

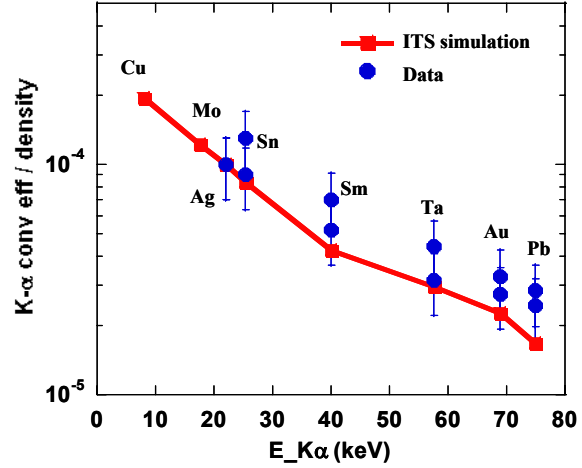


Fig 13. The K- α conversion efficiencies of different target materials. The Monte Carlo simulation using ITS code is plotted.

IV. Exit Plan

Our exit plan is to deliver new radiography experimental techniques and designs to the Programs, specifically, to NIF/HED Material Strength program, Implosion program and Double Shell program. Utilization of m-wire target is extended to Bremsstrahlung radiography to image imploding ignition core to diagnose its symmetry (Compton Radiography.) The LSP modeling capability is not adopted to study Fast Ignition program.

V. SUMMARY

We have obtained high-resolution, high-energy radiographs using high-intensity laser backlighter on μ -flag and μ -wire targets. We find that the high-energy K- α photon emission is confined to the target volume resulting in a spatial resolution in the images defined by the fluor material size. When viewed edge-on and using 5 to 10 μ m μ -wire and μ -flag targets, we obtained spatial resolutions of ~ 10 μ m FWHM. We measured many parameters of K- α conversion efficiencies up to the 75 keV Pb K- α line. At 75 keV, the K- α conversion efficiency, 2.5×10^{-5} , is 4 times lower than the conversion efficiency at 22 keV Ag K- α . Through this LDRD, we made a significant contribution to understanding of physics processes of short pulse laser interactions. The radiography technique developed through this LDRD will be utilized not only by many other programs at LLNL but also other institutions around the world. Our work is recognized by the scientific community. The team members were invited by many scientific conferences and a few papers are published.

VI. INVITED TALKS AND PUBLICATIONS

H. S. Park *et al.*, "High-energy Ka radiography using high-intensity, short-pulse lasers", Phys Plasmas 13, 056309 (2006)

R. Tommasini, et al., “Developing of Compton radiography using high-Z backlighters produced by ultra-intense lasers”, Atomic Processes in Plasmas — ed. J. D. Gillaspay, J. J. Curry, and W. L. Wiese, pp. 248-255 (2007)

H. S. Park et al., “Quasi-isentropic material property studies at extreme pressures : from Omega to NIF”, JPCS (2008).

H. S. Park et al., “High resolution 15 to 100 keV backlighters for HED experiments on NIF”, to be submitted to Phys Plasmas (2008)

H. Park, invited talk at APS/DPP meeting, 2005

H. Park Invited talk at High Temperature Plasma Diagnostics meeting, 2006

R. Tommasini, invited talk at Atomic Process conference, 2007

H. Park invited talk for Plasticity conference, 2007

H. Park, invited talk for International Fusion Sciences and Applications, 2007

REFERENCES

- ¹ L.J. Waxer, D.N. Maywar, J.H. Kelly *et al.*, Optics & Photonics News **16**, 30 (2005).
- ² D.H. McDaniel, M.G. Mazarakis, D.E. Bliss *et al.*, Proceedings of the Fifth International Conference on Dense Z-Pinches, Albuquerque, 2002, edited by J. Davis, C. Deeney, and N.R. Pereira (AIP, Melville, NY, 2002), p.23.
- ³ J.A. Paisner, E.M. Campbell, and W.J. Hogan, Fusion Technology **26**, 755 (1994).
- ⁴ B.A. Remington, G. Bazan, J. Belrak *et al.*, Metall. Mater. Trans. A **35A**, 2587 (2004).
- ⁵ T.R. Dittrich, S.W. Haan, M.M. Marinak *et al.*, Phys Plasmas **6**, No. 5, 2164 (1999).
- ⁶ K.T. Lorenz, M.J. Edwards, S.G. Glendinning, A.F. Jankowski, J.McNaney, M.Pollaine, and B.A. Remington, Phys. Plasmas **12**, 056309 (2005).
- ⁷ M.H. Key, M.D. Cable, T.E. Cowan *et al.*, Phys Plasmas **5**, 1966 (1998).
- ⁸ H.S. Park *et al.*, Phys Plasmas **13**, 056309 (2006).
- ⁹ D. Strickland and G. Mourou, Opt. Commun., **56** 219-221 (1985).
- ¹⁰ M. Sonoda, M. Takano, J. Miyahara and H. Kato, Radiology, **148**, 833 (1983).
- ¹¹ J. Seely et al., High Energy Density Physics 3, 263 (2007).
- ¹² G. Ogura and R. Hack, Medical Device & Diagnostic Industry, March (2006)
- ¹³ A. Friedman, A.B. Langdon, and B.I. Cohen, Comment Plasma Phys. Contr. Fusion **6**, 225 (1981).
- ¹⁴ H. S. Park et al., Proceedings of SPIE, **5196**, 213 (2004)
- ¹⁵ R. Tommasini et al., conference proceedings of Atomic Process in Plasma (2007)
- ¹⁶ K. Yasuike, M.H. Key, S.P. Hatchett, R.A. Snavely, and K.B. Wharton, Rev. Sci. Instrum **72**, 1236 (2001).
- ¹⁷ J. Myatt et al., Phys Plasmas **14**, 056301 (2007).